Journal of Materials Chemistry A

Seawater desalination derived entirely from ocean biomass

Journal Name

ARTICLE TYPE

Seawater desalination derived entirely from ocean biomass[†]

Xiaojie Liu,[a] Yanpei Tian,[a] Yanzi Wu,[a] Andrew Caratenuto,[a] Fangqi Chen,[a] Shuang Cui,[b] Joseph A DeGiorgis,[c,d] Yinsheng Wan,[d] and Yi Zheng[*a]

Solar-driven interfacial evaporation shows great prospects for seawater desalination with its rapid fast evaporation rate and high photothermal conversion efficiency. Here, a sustainable, biodegradable, non-toxic, and highly efficient full ocean biomass-based solar-driven evaporator is reported, which is composed of chitosan (CS) hydrogel as the hydratable skeleton and cuttlefish ink (CI) as photothermal material. Under solar irradiation, the cuttlefish ink powder harvests solar energy and heat the surrounding water. Simultaneously, the water in the three-dimensional network of chitosan hydrogel is rapidly replenished by the interconnected porous structure and the hydrophilic functional groups attached to the polymer chains. With its enlarged evaporation surface, high solar absorptance, adequate water transportation, good salt drainage, and heat localization, the CI/CS-based evaporator achieves a remarkable evaporation rate of 4.1 kg m^{-2} h^{-1} under one sun irradiance (1 kW m^{-2}) with high-quality freshwater yields. This full ocean biomass-based evaporator with abundant raw material availability provides new possibilities for an efficient, stable, sustainable, and environmentally friendly solar evaporator with guaranteed water quality.

1 Introduction

The scarcity of freshwater is quickly becoming a predominant concern for human life and sustainable development[1]. Solar-driven steam generation, whereby abundant solar energy is harvested as a heat source used to purify water directly from seawater, is emerging as an environmentally benign and sustainable approach to mitigate the worldwide water crisis, due to its high energy conversion efficiency. In the past few years, tremendous research efforts have been made to realize highly efficient solar-driven interfacial evaporation performances. These efforts have concentrated on the amelioration of device design and the development of advanced materials to enhance solar absorptance, thermal management, water transport, and vapor diffusion[2–8]. From the perspective of energy efficiency, the logical design of an interfacial evaporation device should integrate the following components into one system: (1) photothermal materials having efficient absorption of solar radiation and efficiently converting the radiation into heat; (2) evaporation structures which can simultaneously enlarge the evaporation surface and supply water

to the heated area; and (3) thermal insulators to reduce the heat loss to the bulk water and ambient air.

Thus far, immense progress has been made on the development of material platforms, including photothermal materials[9–13] and hydrophilic supporting substrate materials[14–17]. These advances are leveraged when composing the evaporator − the core component of the evaporation device. Photothermal materials mainly consist of either carbon-based materials, plasmonic metal nanoparticles, and semiconductor materials, while the hydrophilic substrate materials typically include hydrogels or hydrophilic sponges. However, high-cost raw materials, complicated fabrication processes, and weak long-term stability will all hinder the widespread use of these materials in practical applications. Furthermore, many synthetic polymers are not environmentally friendly nor biodegradable, and the disposal of these materials poses a significant concern to the environment. Hence, an increasing level of environmental awareness has motivated the research community to seek more green materials which can be applied in the water purification and treatment.

With respect to sustainable development, biomass materials are highly attractive for solar-driven steam generation due to their biocompatibility, renewability, and sustainability[18–24]. A growing number of evaporators are completely or partially composed of natural materials, such as wood[25,26], algae[27], mushrooms[28] and waste rice straw[29], which are often carbonized or serve as supporting materials when combined with thermal materials. Al-

[a] *Department of Mechanical and Industrial Engineering, Northeastern University, Boston, MA 02115, USA. E-mail: y.zheng@northeastern.edu*
[b] *National Renewable Energy Laboratory, Golden, CO 80401, USA.*
[c] *Whitman Center, Marine Biological Laboratory, Woods Hole, MA 02543, USA.*
[d] *Department of Biology, Providence College, Providence, RI 02918, USA.*
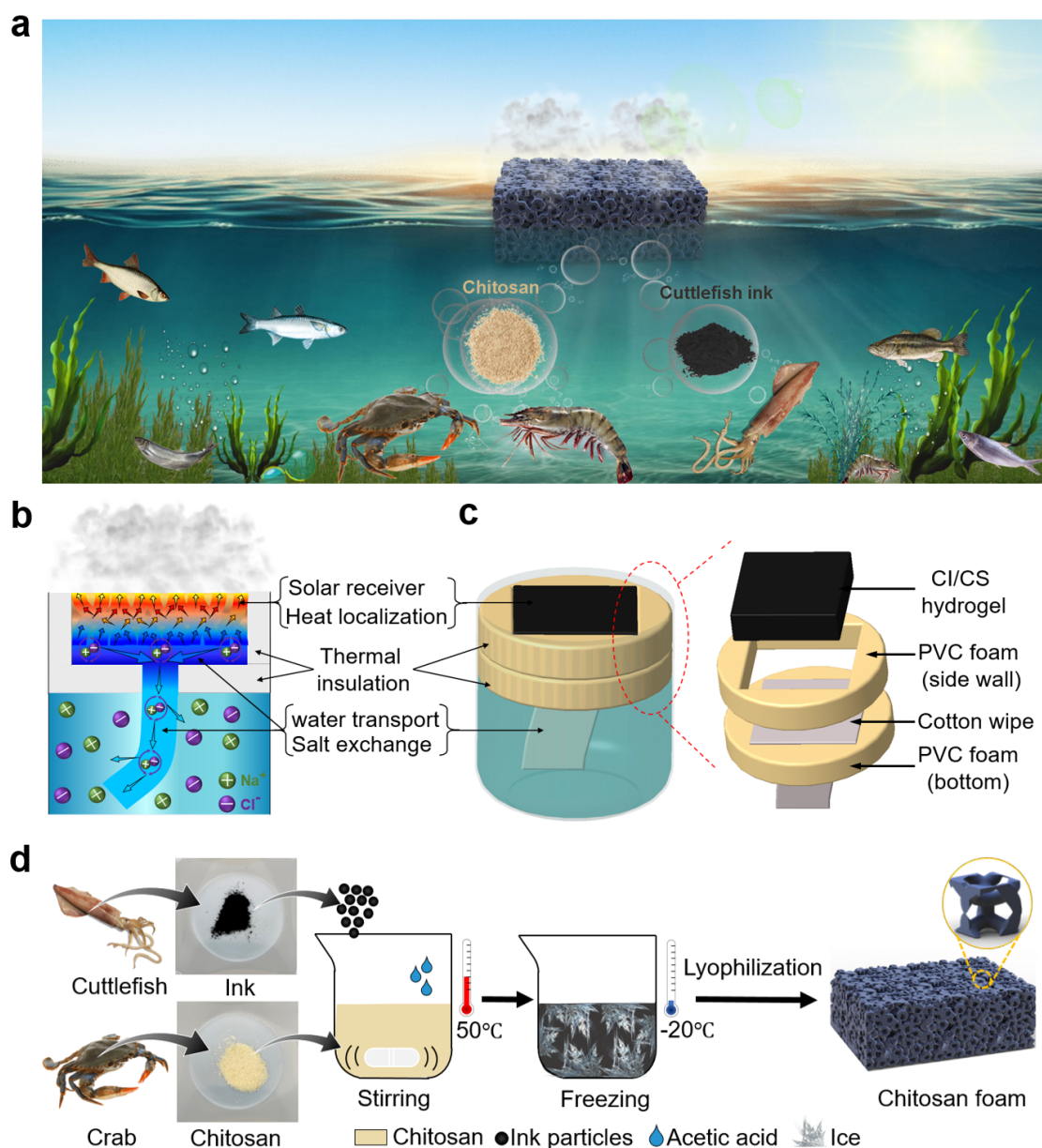
Fig. 1 Schematic of the cuttlefish ink/chitosan (CI/CS) hydrogel for solar-driven steam generation. (a) Schematic illustration of the CI/CS evaporator employed in solar-driven desalination. Under one sun illumination, the CI/CS hydrogel-based evaporator floats on the sea to produce freshwater directly from seawater by absorbing solar energy. The main raw materials used to make the CI/CS evaporator include the hydrogel and photothermal materials all come from marine life. The cuttlefish ink nanopowders (the pile of black powders), produced by cuttlefish, act as the photothermal materials to efficiently absorb solar irradiation and convert it into heat. The CS (the pile of beige powders), extracted from shellfish, is built into a three dimensional interconnected porous structure selected as the skeleton. (b) Schematic of the steam generation mechanism of the CI/CS hydrogel-based evaporator converting the bulk saltwater into pure water vapor using sunlight. Strong interfacial steam generation occurs, which is powered by solar energy. The solar-thermal heat generation is localized in a narrow strip near the air/liquid interface. Sufficient water is pumped to the porous evaporator through the super hydrophilic materials connecting the evaporator and the bulk water, and salt is excreted via the water path. The thermal insulator reduces downward conduction heat loss and surrounding convection heat loss from the evaporator to the underlying bulk water and ambient air, respectively. (c) Schematic of the experimental set-up for the solar-driven steam generation via the CI/CS hydrogel with excellent water absorption and photothermal performance. (d) Schematic illustration of the fabrication process of CI/CS hydrogel.

though biomass materials provide an environmentally friendly solution, challenges still remain within the application of these biomass-based evaporators. These green solutions often suffer from relatively low evaporation rates, as well as salt accumulation which blocks the water transport path and impedes solar absorption. As such, there is still much room for improvement in the use of biomass materials in steam generation.

Chitosan (CS) is a type of polysaccharide material obtained from the N-deacetylation of chitin, which is one of the most abundant amino polysaccharide found in nature and is mainly extracted from the shells of crustaceans (such as crabs and shrimp)[30,31]. The chitosan hydrogel, with a three-dimensional

network, exhibits excellent hydrophilicity and water absorption, which arise from the hydrophilic functional groups in polymeric chains and the interconnected porous structure, respectively. Featuring the beneficial properties of hydrophilicity, biocompatibility, biodegradability, and nontoxicity, this chitosan hydrogel has displayed immense value as a supporting material for biomass-based evaporators used for the solar-driven desalination. In addition to the chitosan hydrogel serving as a supporting substrate, the ocean also provides a desirable ocean biomass-based photothermal material - cuttlefish ink. Notably, cuttlefish ink (CI) consists of natural melanin particles with great broadband high solar absorption, making it a suitable candidate for photothermal material platforms. Moreover, cuttlefish ink particles have good dispersibility in water due to the hydrophilicity of the ink particles, allowing cuttlefish ink particles to mix evenly with supporting materials [32]. In this study, we demonstrate a full ocean biomass-based CI/CS evaporator comprising chitosan hydrogel and cuttlefish ink for high-efficiency solar-driven desalination, as shown in Fig. 1a, which is both derived from and applied to the ocean. The chitosan-based aerogel, boasting low thermal conductivity, serves as the supporting substrate to continuously supply adequate water to the top heating layer through its interconnected porous structures via capillary pumping and swelling effects. In addition to the water pumping, the chitosan hydrogel also acts as a thermal barrier to localize the solar heating effect in the narrow area near the air/liquid interface (Fig. 1b). The other core component of our evaporator − the photothermal material − is made of cuttlefish ink particles. The cuttlefish ink particles, which easily adhere to the supporting substrate, effectively absorb solar energy and convert it into heat to generate vapor at the heating layer. Meanwhile, the macroporous structure of the chitosan hydrogel assists ample generated vapor in diffusing out. To pursue a more favorable desalination performance, as shown in Fig. 1c, the evaporator is integrated into a typical evaporation device, including the evaporator, insulation foam (Polyvinyl chloride (PVC) foam), and a water pathway (cotton wipe), to further restrict the conduction heat loss to the underlying bulk water and convection heat loss to the ambient air during desalination process. This evaporation device has achieved an evaporation rate as high as 4.1 kg m^{-2} h^{-1} under one sun irradiation, making it stand out amongst not only biomass-based evaporation devices, but also amongst many two-dimensional evaporation devices.

2 Experimental section

2.1 Materials

Chitosan with medium molecular weight and a deacetylation degree of 75 - 85%, acetic acid, sodium chloride (NaCl, 99.0%), and sodium hydroxide (NaOH) are all purchased from Sigma-Aldrich, USA. All chemicals are directly used as received without further purification. Pure cuttlefish ink powder is purchased from Fluxias GmbH Ltd, Germany. The cotton wipe used is supplied by Webril. The PVC insulation foam is purchased from McMaster-Carr.

2.2 Characterization

The reflectance spectra (UV-Visible-Near-infrared range: 300 nm ~ 2500 nm) are measured by the Jasco V770 spectrophotometer at an incident angle of 6° with the ISN-923 60 mm BaSO$_4$ based integrating sphere equipped with PMT and PbS detectors. The reflectance spectra are normalized by a PTFE based reflectance standard. The reflectance spectra at different AOI are characterized by using wedges of different angles at the sample port of the Jasco V770 spectrophotometer. The transmittance spectra (Mid-infrared region: 2.5 μm ~ 20 μm) are measured by the Jasco FTIR 6600 spectrometer at a normal incident angle with reference to the background spectrum of a hydraulic pressed KBr film (20 psi). The compressive test for the CI/CS hydrogel is conducted by using a RSA-G2 Solids Analyzer (TA Instruments) at a compression rate of 3 mm min^{-1} at room temperature. The Raman spectrum is measured via a Raman spectrometer equipped with a 532 nm laser source (LabRAM HR800, Horiba Jobin Yvon). The Extech EC400 ExStik salinity meter is utilized to characterize the water quality of the collected water samples. Infrared images of samples are taken employing the FLIR A655C thermal camera at a resolution of 640 × 480 with a 25° lens. The thermal conductivity of samples is characterized by the Hotdisk TPS 2500 S. The contact angle of samples is measured by SINDIN SDC-350 contact angle meter.

2.3 Preparation of CI/CS hydrogel

The CI/CS hydrogel was prepared following a previously reported procedure [33]. Both the chitosan powder (0.5 g, 1 g, and 1.5 g) and cuttlefish ink powder (0.75 g, 1.5 wt% in deionized (DI) water) were dispersed in 0.2 M acetic acid (50 ml) with magnetic stirring at 50°C for 4 hours forming a homogeneous black chitosan solution (1 wt%, 2 wt%, and 3 wt%). The obtained chitosan solution was cast into an aluminum tin (35 mm in diameter) and transferred into a freezer at –20°C overnight to solidify the solution. The solidified sample was lyophilized at –75°C until all solvent was completely removed leaving a black CI/CS-based aerogel. To get the CI/CS hydrogel, the aerogel was soaked into 0.5 M NaOH solution for 2 hours, followed by flushing several times with DI water. The chitosan hydrogel was fabricated following the same procedure without cuttlefish ink powder.

2.4 Solar steam generation experiments

The steam generation experiments are carried out under a solar simulator (Newport, 94081A, class ABB) which supplies solar flux of 1 kW m^{-2} with an optical filter for the standard AM 1.5 G spectrum. Solar intensity at the position of the CI/CS-based evaporator is measured by a TES 132 solar power meter. DI water and NaCl solutions with various concentrations are prepared at the same initial temperature of 19°C and placed in a plastic beaker with an inside diameter of 48 mm. Before the crosslinking process, the dry aerogel is cut into the thickness of 7 mm. The CI/CS-based evaporator, tightly surrounded by PVC foam with the same thickness, is placed on the PVC foam underneath which center is penetrated by a strip of cotton wipe. To accurately monitor the mass of the water, the evaporation device is placed on an electric
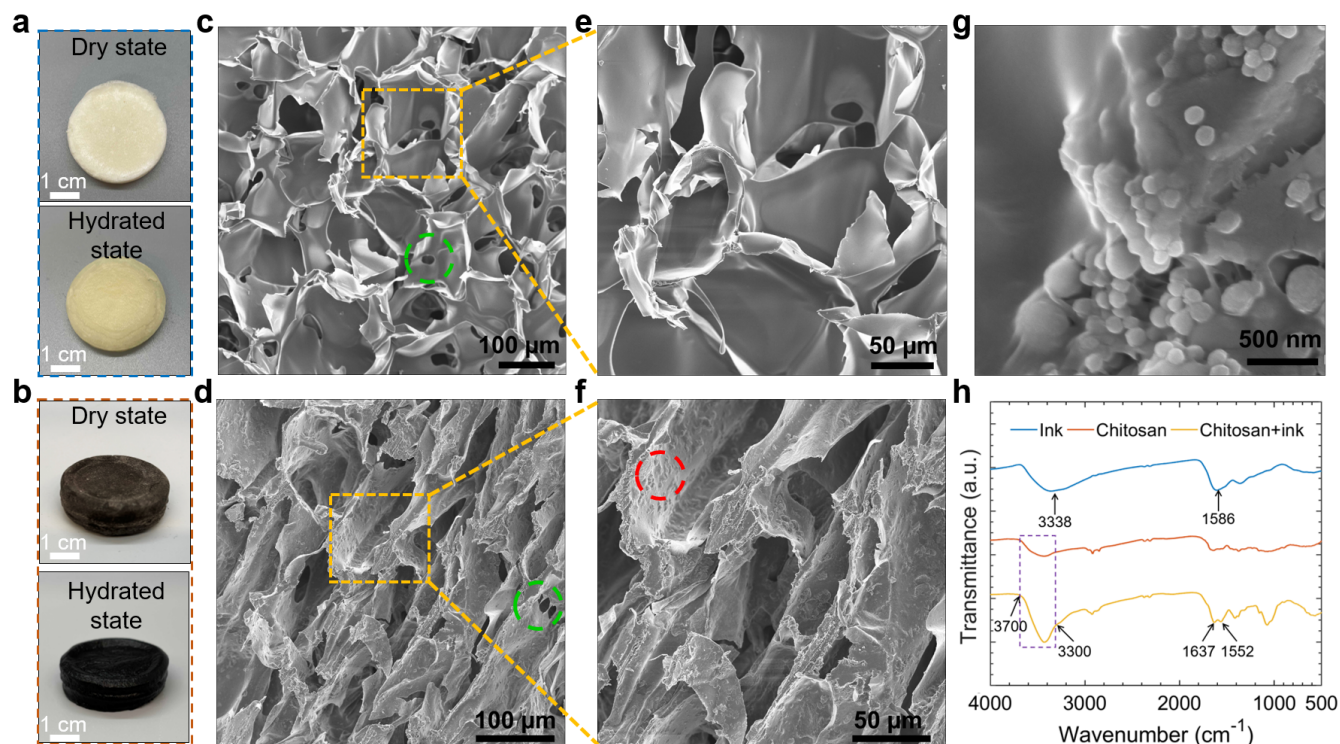
Fig. 2 Characterization of the CI/CS porous structure. Photographs of CS-based hydrogels (a) and CI/CS-based hydrogels (b) with diameters of 34 mm at dry and hydrated states, respectively. (c–f) Scanning electron microscopy (SEM) images of the CS-based aerogel and CI/CS-based aerogel with micro-sized porous structures, respectively, at different magnifications. The green dashed circles in (c) and (d) show the smaller pores on the wall of frame. The red dashed circle in (f) shows the rugged surface of the CI/CS-based aerogel resulting from the accumulation of ink particles. (g) SEM image of cuttlefish powders. (h) Fourier transform infrared (FTIR) spectra of cuttlefish ink powders, chitosan powders, and mixture of both showing the responding chemical composition.

balance (RADWAG, PS 1000.X2.NTEP) with a resolution of 0.001 g connected to a computer which enables the recording of the real-time mass change. The real-time temperature is monitored by an infrared radiation camera (FLIR, A655sc).

3   Results and discussion

3.1   Fabrication and characterization of the full ocean biomass-based evaporator

Chitosan is a linear cationic polysaccharide obtained by the partial deacetylation of chitin, the second most abundant biopolymer available in nature after cellulose [34–36]. Chitin occurs in different profuse nature sources, as an important constituent of the exoskeletons of crustacea, mollusks and insects as well as in the cell walls of certain fungi. Principally, it is extracted from the shell waste of shrimps, lobsters, and crabs. There are two major functional groups, namely amino group (–NH$_2$) and hydroxyl group (–OH), along the chitosan chain, which are able to form hydrogen bond with the O-atom and the H-atom of water molecule, respectively. In addition, chitosan is generally soluble in dilute aqueous acidic solutions. At low pH, the free –NH$_2$ groups on the chitosan chain are protonated into the soluble –NH$_3^+$, enabling the chitosan to dissolve easily in acidic solution. On the other hand, chitosan remains insoluble in water and alkaline solutions due to the fact that the free –NH$_2$ groups can not be protonated in neutral and alkaline medium [37]. The fabrication process of the CI/CS hydro-

gel is shown in Fig. 1d. Briefly, chitosan powder and cuttlefish ink powder were dissolved in an acetic acid solution with stirring and mild heating at 50°C for four hours to form a homogeneous black mixture. The black non-Newtonian fluid was then frozen at –20°C overnight. After a conventional lyophilization procedure, in which the ice crystals inside the frozen composite were removed by sublimation of ice crystals, the CI/CS-based porous structure was obtained.

The black color of the CI/CS hydrogel is attributed to cuttlefish ink powders which are distributed uniformly inside the chitosan hydrogel network (Fig. 2a and b). The main constituent of cuttlefish ink is melanin, a naturally occurring black pigment with good light absorption across a broad spectrum of wavelengths [38]. Scanning electron microscopy (SEM) is implemented to characterize the structure of the fabricated hydrogel after freeze-drying with an uniform porous structure. The CS-based hydrogel shows a rough surface with a flake-sheet like structure. These flakes have smooth surfaces (Fig. 2c and e) and are interconnected to form porous structures together with small pores (15 μm ∼ 20 μm, green dashed circles), which facilitate the pumping of sufficient water from the bulk reservoir to the evaporation surface. Moreover, these interconnected pores also function as salt rejection channels, efficiently dissipating salt to the bulk reservoir. Compared with the smooth surface of these flake sheets in CS-based hydrogel, the CI/CS-based hydrogel has small bumps on intercon-
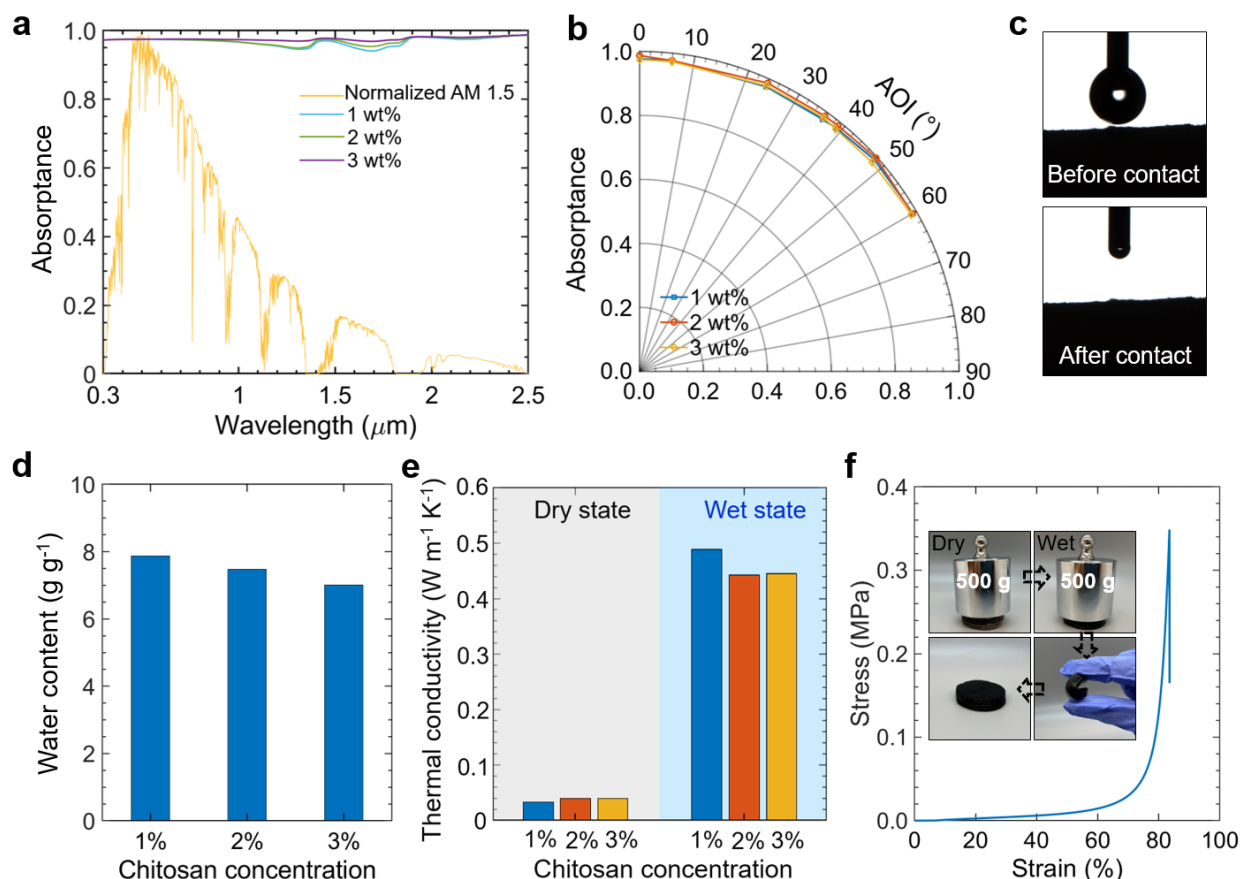
Fig. 3 Characterizations of the CI/CS hydrogel foam. (a) The absorptance spectra of the CI/CS hydrogel displaying against the AM 1.5 spectral solar irradiance spectrum. (b) The average solar absorptance of the CI/CS hydrogel foams across different angles of incidence from $0°$ to $60°$. (c) Dynamic contact angle of the CI/CS hydrogel. (d) Water absorption ratios of the CI/CS hydrogels with different chitosan concentration. (e) Thermal conductivity of different CI/CS hydrogel foams in dry and wet state. (f) Compressive stress-strain curve of the 3 wt% CI/CS hydrogel. The insets are photographs exhibiting the good toughness, compressibility and recoverability of the CI/CS hydrogel foam both in dry and wet states during compression and bending tests.

nected channel walls due to the embedded ink particles. These walls serve as excellent sunlight traps to boost the photothermal effect (Fig.2d and f). Ink particles with diameters of around 115 nm are effective photothermal materials to absorb sunlight and convert it into heat (Fig. 2g). Fourier transform infrared (FTIR) spectra elucidate the chemical compositions of CI/CS-based hydrogel (Fig. 2h). The broad absorption bands from 3,300 cm^{-1} to 3,700 cm^{-1} are attributed to the stretching vibration of the combined peaks of $-NH_2$ and $-OH$ groups of chitosan, indicating the hydrophilic features of the pure CS-based hydrogel and CI/CS-based hydrogel. The peaks at 1,637 cm^{-1} and 1,552 cm^{-1} are ascribed to the $CONH_2$ and NH_2 groups, respectively[39]. The broad absorption at 3,338cm^{-1} results from the $-OH$ groups of melanin, and the peak at 1,586 cm^{-1} comes from the symmetric carboxylate stretching vibrations (COO^-)[40]. The hydrophilic feature of melanin due to the $-OH$ groups enhances the water absorption of CI/CS-based hydrogel.

3.2 Materials characterizations

One of the key aspects critical to achieving a solar-driven high evaporation rate is to efficiently absorb the solar irradiance. At-

tributed to the melanin constitute existing in cuttlefish ink and the porous outer surface of the hydrogel network, the CI/CS hydrogel shows a high solar absorptance across the solar wavelengths in the wet state and renders the CI/CS hydrogel into a perfect solar absorber, allowing for the harvesting and conversion of sunlight into thermal energy (Fig. 3a). Moreover, the solar absorptance of the wet CI/CS hydrogel is angle-independent even at large incident angles, e.g., $60°$, indicating that the CI/CS hydrogel can absorb sunlight effectively at any time of the day, making it suitable for most regions of the world (Fig. 3b). To achieve a satisfactory evaporation performance, a continuously available water supply is critical for a evaporator. The wetting performance of the CI/CS hydrogel is measured by the dynamic contact angle. As shown in Fig. 3c, the water droplet disappears instantly as soon as it touches the upper surface of CI/CS hydrogel, which results from the hydrophilicity of the chitosan hydrogel and the strong capillary effects resulting from the interconnected porous structure network. This provides a high water absorption ratio over 7 g g^{-1} (Table S2†), that is significantly higher than that of other biomass-derived materials, e.g., carbonized wood (2.3 g g^{-1}) (Fig. 3d and S1†). The exceptional water absorption capa-
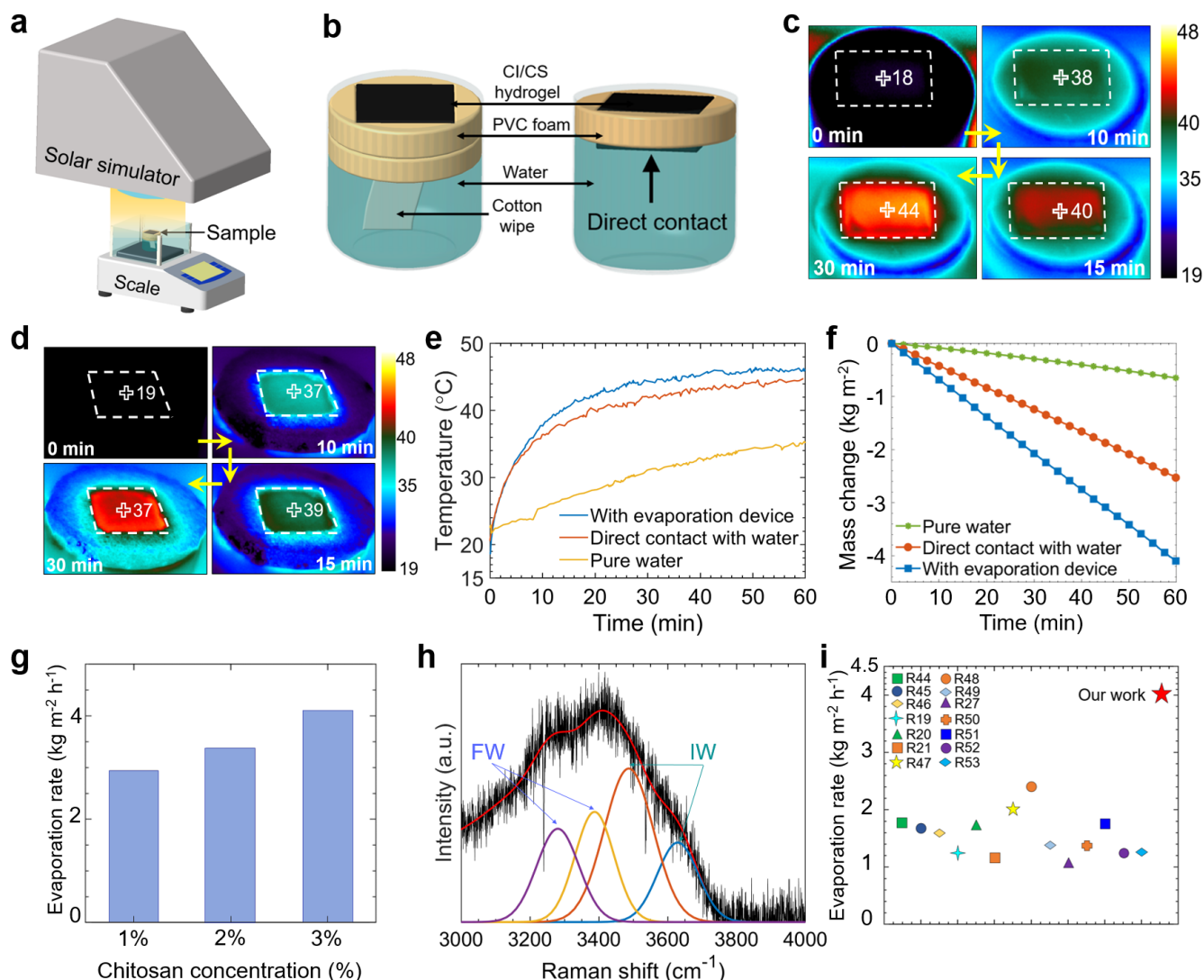
Fig. 4 Experimental apparatus and solar steam generation performance of the CI/CS hydrogel evaporator. (a) Schematic illustration of the setup for the steam generation experiment involving the solar simulator, electrical balance, and our hydrogel evaporator. (b) Schematic showing the water supply methods of a cotton wipe as a water path (left) and direct contact with water (right). The infrared images exhibiting the temperature distribution of evaporator top surface with two different water supply methods: (c) the cotton wipe serving as the water path, (d) the CI/CS hydrogel directly contacting the water. The unit of temperature in the infrared images is °C. (e) Temperature evolutions of the CI/CS hydrogel with different water supply methods and the pure water under one sun illumination within initial 60 minutes. (f) Mass changes of the pure water and the CI/CS evaporator with different water supply methods after the evaporation device is in the stable state. (g) Evaporation rates of the evaporator fabricated with different concentrations of chitosan. (h) Raman spectrum and the fitting curves of water in the 3 wt% CI/CS hydrogel. The solid black curve and the red solid curve indicate raw data of the Raman spectrum and the cumulative fitted curve, respectively. The solid purple, yellow, orange, and blue curves are the fitting curves through Gaussian function. The FW and IW denote the free water and the intermediate water, respectively, in the CI/CS hydrogel. (i) The water evaporation rate of CI/CS hydrogel-based evaporation device comparison with other biomass-derived evaporator. Details are listed in Table S3†.

bility ensures that the CI/CS hydrogel will effectively pump water to the top interfacial evaporation surface. The thermal conductivity of the dry CI/CS hydrogel is also very low (around 0.04 W m^{-1} K^{-1}), resulting from the introduced air inside the pores of the hydrogel foams acting as a natural insulator (Fig. 3e). After absorbing water, the thermal conductivity increases over 10 times to around 0.46 W m^{-1} K^{-1}, which elucidates that the hydrogels intake water effectively, as this approaches the thermal conductivity of water (0.6 W m^{-1} K^{-1}). The compressive strength of the CI/CS hydrogel is tested, which quantitatively demonstrates the

mechanical property, and the representative stress-strain curve is shown in Fig. 3f. The compression strength of 0.35 MPa is recorded at a large fracture strain of 83.5%, which allows for a high deformability and indicates a good flexibility and elasticity of the hydrogel. The CI/CS hydrogel is also mechanically robust, withstanding more than 500 times of its weight without obvious deformations in the dry state. The wet hydrogel elastically deforms under the compression (500 grams weight loading) and bending tests, but retains its original structure after the removal of the weight loading and the external force. The flexibility of the

wet hydrogel expands its potential applications, such as deployment on curved surfaces.

3.3 Solar-driven steam generation performance

The solar-driven steam generation performance is evaluated by measuring the mass change of water under one sun irradiance at a room temperature of around $21°C$ and relative humidity of 30%. The experimental setup for evaluating the mass change of the solution and temperature evolution of the 3 wt% CI/CS hydrogel under a one sun irradiance is schematically elucidated in Fig. 4a. The evaporation device is placed in the center of the illumination beam of the solar simulator to provide it with the maximum possible collimated light (Fig. S2†). To quantitatively characterize the performance of the CI/CS hydrogel as a 2D evaporator, we ensure that the top surface is the only water evaporation and light absorption surface. To do so, the CI/CS hydrogel is surrounded tightly by PVC foam with the same thickness as a sample. This layer serves as a thermal insulation layer with closed pores, and prevents the escape of vapor from sidewalls and localizes heat to the sample. The wrapped hydrogel is placed on a PVC foam layer, which is crossed by a strip of cotton wipe with super hydrophilicity in the center, to reduce the downward conduction heat loss from the hydrogel to the bulk water beneath (Fig. S3†). The porous structure and intrinsic hydrophilicity of cotton wipe making it a proper water path in a evaporation device to efficiently support water to the evaporator (Fig. S4†). Due to the micro-sized interconnected porous structure of the hydrogel and the strong hydrophilicity of chitosan, the CI/CS hydrogel is able to continuously gain sufficient water supply from the cotton wipe strip which serves as a water path, ensuring efficient water evaporation (Fig. 1c and 4b, left). In order to highlight the importance of the cotton wipe and PVC foam water supply method to the evaporation performance, the wrapped CI/CS hydrogel is placed on top of water which is in direct contact with the bulk water (Fig. 4b, right). The evaporation performances with these two different water supply methods are shown by the temperature evaluations and mass changes of water. To preliminarily evaluate the evaporation performance of a CI/CS hydrogel evaporator, a typical vapor generation test is usually conducted under constant solar illumination for 90 minutes, and the first 30 minutes is regarded as a pre-heating stage, allowing the CI/CS hydrogel evaporator to reach a stable working state. As shown in Fig. 4c and d, infrared images are used to monitor the temperature distribution during the steam generation process once the light is on. The top surface temperature of the CI/CS hydrogel with a cotton wipe as water path climbs rapidly up to $44°C$ in 30 minutes, while the evaporator with direct contact to water can only reach $37°C$ within the same time period. Note that the temperatures marked in the figures are the central point temperature of hydrogel. Figure 4e shows the central temperature evolutions for different samples within the initial 1 hour. The stagnation temperature of the top surface of the hydrogel on the cotton wipe is $46°C$, which is about $10°C$ higher than that of pure water. Obviously, the hydrogel with direct contact with water has an overall temperature drop due to the heat loss from the hydrogel to the bulk water. This illustrates

the advantage of employing the cotton wipe as a water path and the PVC foam as a thermal barrier to localize the heat at the evaporation interface. The rapid photothermal response and excellent heat localization of the evaporator design will remarkably boost freshwater yields in real-life applications.

The mass changes of the CI/CS hydrogel evaporator with different water supply methods under one sun are illustrated in Fig. 4f compared with the pure water. The mass changes of water with different samples are recorded for the last 1 hour among the 90-minute vapor generation test. The complete recorded mass change data is shown in Fig. S5†. The evaporation rate of the CI/CS hydrogel evaporator with the cotton wipe as a water path is 4.1 kg m^{-2} h^{-1}, which is much higher than the case with direct contact with water (2.5 kg m^{-2} h^{-1}), and is also 6.3 times of the pure water (0.65 kg m^{-2} h^{-1}). It is noteworthy that even in the case of direct contact with bulk water, where there exists nonnegligible conductive heat loss to the water sink, the evaporator still exhibits an outstanding evaporation performance with a evaporation rate of 2.5 kg m^{-2} h^{-1}, which still stands out amongst the 2D evaporation devices. The CI/CS hydrogel fabricated with 3 wt% chitosan solution shows the highest evaporation rate of 4.1 kg m^{-2} h^{-1}, whereas the others with chitosan concentrations of 1 wt% and 2 wt% show slightly reduced values of 2.94 kg m^{-2} h^{-1} and 3.38 kg m^{-2} h^{-1}, respectively (Fig. 4g). The evaporation rate of the CI/CS hydrogel evaporator is much higher than the theoretical limit (1.47 kg m^{-2} h^{-1} [41]) under one sun, which comes from the expanded evaporation surface, owing to the porous structure coming from lyophilization. More importantly, because of the water-polymer interaction, water in the hydrogel requires less energy input compared with bulk water for vaporization owning to the existence of a large proportion of intermediate water in hydrogel. Water in the CI/CS hydrogel performs the different intermolecular hydrogen bonding, which can be classified as water/polymer bonding, normal water/water bonding, and weakened water/water bonding. Accordingly, water is in existence as bound water, free water (FW), and intermediate water (IW) in the CI/CS hydrogel. Bound water is usually composed of water molecules which possess strong interaction with functional groups in polymer chains. In contrast, free water is usually associated with water molecules that have negligible interaction with polymer chains, which has a structure similar to that of bulk water. Intermediate water exists between bound water and free water, and has weak interaction with polymer chains, as well as adjacent water molecules respectively [14,42,43]. Note that the weakly interacted intermediate water requires less energy to escape from surroundings in the hydrogel compared with bulk water. As shown in Fig. 4h, the Raman spectrum in the frequency region of O−H stretching modes is fitted into four peaks via the Gaussian function, where the peaks are observed at 3,281 cm^{-1}, 3,387 cm^{-1}, 3,487 cm^{-1}, and 3,629 cm^{-1}, respectively. Specifically, the peaks at 3,281 cm^{-1} and 3,387 cm^{-1}, which are associated with free water, arise from the collective in-phase vibrations of all molecules in the aggregate and the out-of-phase mode of O−H stretching, respectively. The other two peaks at 3,487 cm^{-1} and 3,629 cm^{-1} are attributed to the symmetric and asymmetric stretching of the weakly hydrogen bounded interme-
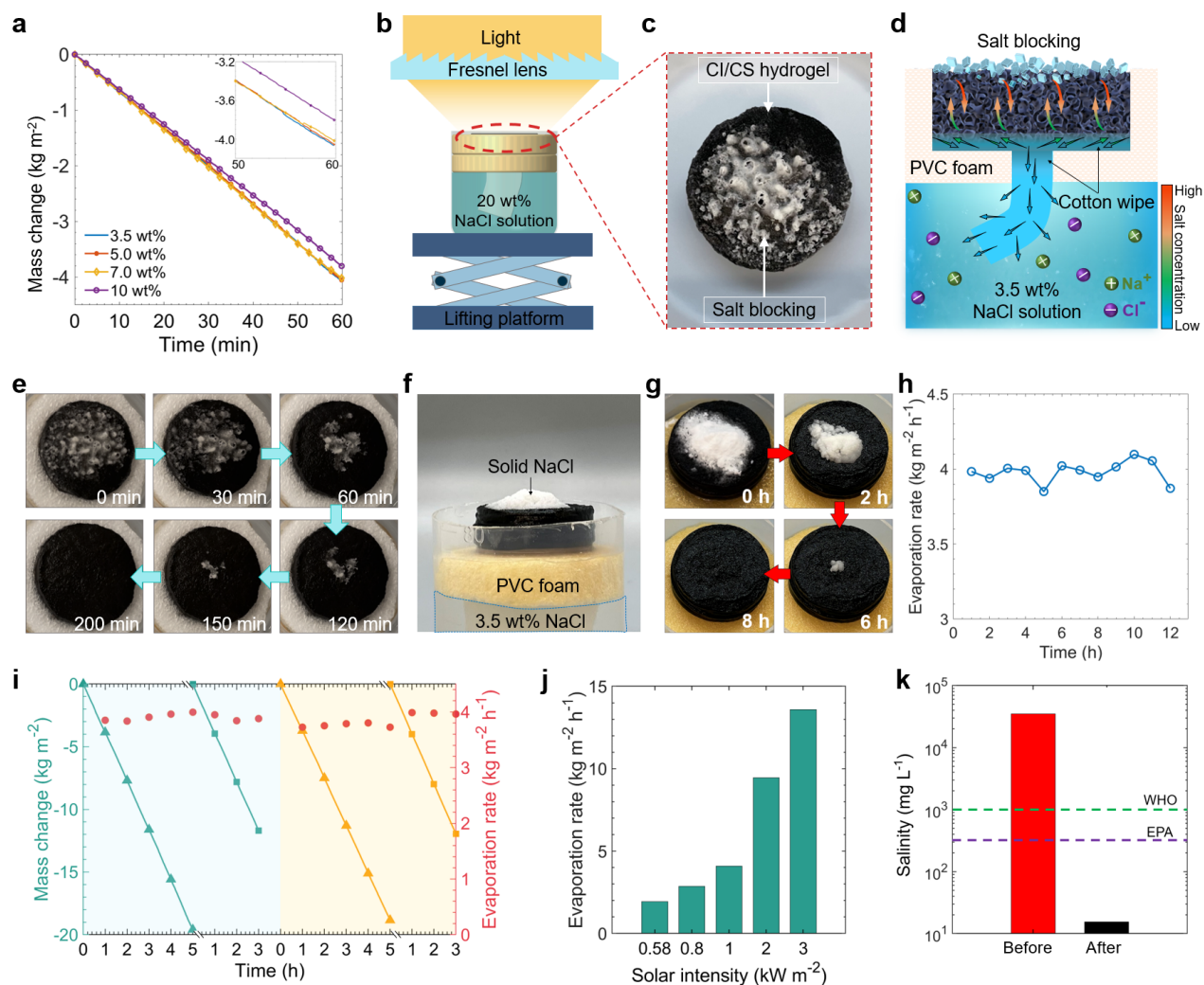
Fig. 5 Solar desalination and salt rejection performance of the CI/CS hydrogel evaporator. (a) Mass change of the CI/CS evaporator in solutions with different salinities. Inset shows the mass changes from 50 minutes to 60 minutes. (b) Schematic illustrating the experimental setup for salt accumulation under the concentrated sunlight. (c) Top view showing the accumulated salt on the top surface of the CI/CS evaporator after 60 minutes with 20 wt% NaCl solution as the water supply. (d) Schematic elucidating the working process of the salt rejection for CI/CS evaporator with the 3.5 wt% NaCl solution. (e) Time-lapse photographs of the salt dissolving process on the top surface of the CI/CS evaporator. (f) Photograph of the experimental setup of the salt rejection experiment with added salt. (g) Salt-rejection experiment showing the excellent salt-dissipation functionality of the CI/CS evaporator. (h) Evaporation rates of the CI/CS evaporator over 12 cycles. (i) Mass changes and the corresponding evaporation rates of water for the CI/CS hydrogel evaporator using the 3.5 wt% NaCl solution over two 8-hour periods. (j) Evaporation rate of the CI/CS evaporator under solar intensities of 0.58, 0.8, 1, 2, and 3 kW m^{-2}, respectively. (k) Salinity of the water before and after desalination.

diate water, respectively. Moreover, the intensity of the Gaussian components provides information on the relative ratio of two types of water structure, the free water and intermediate water. According to the fitting curves, as depicted in Fig. 4h, the ratio of intermediate water to free water is 1.31, indicating that intermediate water accounts for a high proportion in the CI/CS hydrogel.

The water evaporation enthalpy is temperature-dependent. To evaluate the equivalent evaporation enthalpy of water in the CI/CS hydrogel evaporator at its operating temperature (43°C), the dark environment experiment during which the evaporation surface temperature of the CI/CS hydrogel evaporator and the pure water are both 43°C in a dark room (21°C). The detailed experimental process is provided in the Fig. S6†. The photothermal efficiency, η_{pt}, of the CI/CS evaporator can be calculated using

the equation

$$\eta_{pt} = \dot{m}h_{equ}/Q_s \qquad (1)$$

where $\dot{m}$ is water evaporation rate, h_{equ} is the equivalent vaporization enthalpy of the water, and Q_s refers to power density of the incoming light illumination. A photothermal efficiency of about 72.94% is demonstrated for 3 wt% CI/CS evaporator and the detailed calculation process and the heat loss analysis are shown in the ESI†. The comparison of the evaporation rate of this CI/CS hydrogel evaporator with other published biomass derived materials are listed in Fig. 4i and Table S3†[19–21,27,44–53].

3.4 Solar desalination and salt-rejection performance of the CI/CS hydrogel evaporator

Salt rejection capabilities and suitable water quality after desalination are essential for solar-driven desalination applications, especially in high-salinity water. Salt accumulation in water channels will block continuous water pumping and subsequent salt drainage. Moreover, the accumulated salt on the evaporation surface reflects sunlight, which reduces harvested energy, and dramatically decreases water evaporation performance and simultaneous salt rejection. Therefore, it is significant to develop materials with excellent salt-dissipation functionality, particularly for implementations in high-salinity environments. The effects of different salt concentrations on the evaporation rates of the CI/CS porous evaporator are shown in Fig. 5a. Ascribing to the sufficient water supply to the heating surface and the interconnected porous structure of hydrogel, no visible salt accumulations are observed during the experiment, even when using the 10 wt% NaCl solution as the bulk water under one sun irradiation. The evaporation rate stabilizes at 4.0 kg m^{-2} h^{-1} when the salt concentrations increase from 3.5 wt% to 7 wt%. The rate, decreases slightly to 3.8 kg m^{-2} h^{-1} when the salinity of the bulk water is as high as 10 wt%, which shows great promise for desalination in high-salinity brine (Fig. 5a inset). This stable evaporation performance of CI/CS hydrogel with various salinities is attributed to the excellent salt rejection capabilities of the CI/CS evaporator, which are highly desired in solar desalination applications.

To evaluate the salt self-cleaning capability of the CI/CS hydrogel evaporator, simulated salt accumulation process on the evaporation surface is conducted under concentrated solar irradiance with a high-salinity water supply. Figure 5b shows the experimental setup for salt accumulation, including a solar simulator as the light source, a Fresnel lens to concentrate sunlight, a lifting platform for adjusting the distance between the evaporation surface of the CI/CS hydrogel evaporator and the Fresnel lens. A 20 wt% NaCl solution is employed as the water source to accelerate the salt accumulation process. A solar intensity of 10 kW m^{-2} irradiates on the surface of the CI/CS hydrogel evaporator, during which the focused sunlight heats the top surface of the CI/CS hydrogel evaporator, and water continuously evaporates. When the evaporator is exposed to the concentrated light, the salt water on the evaporation surface continuously occurs intense water vaporization, evaporating a lot of water vapor and making the salinity of remaining water increase in short time. Then, the salt crystals are gradually formed and accumulated on the evaporation surface. Salt blockage of the CI/CS hydrogel evaporator happens when the evaporation rate and the salinity of the bulk water are high. The salt residual cannot be efficiently rejected to the underlying bulk water because the salt concentration difference between evaporation surface and underlying bulk water becomes smaller, even the higher concentration appears on the top surface as the evaporation progresses. Generally, the CI/CS hydrogel evaporator cannot be blocked by the salt crystals due to its porous structure and efficient water supply to drive the salt back downward to the bulk water. However, under the situations of concentrated sunlight and high-salinity water, more salts need to

be dissipated from the evaporation surface that is more than the salt rejection capability of the CI/CS hydrogel evaporator. The salt crystal blocks the pores of the CI/CS evaporator, then the driven force from the capillary phenomena becomes weak, and the underlying low-salinity water cannot be pumped up to dissolve the salt residual.

After 60 minutes, salt crystals cover most of the top surface of the CI/CS hydrogel evaporator (Fig. 5c). Then the solar simulator is shut down, the CI/CS hydrogel evaporator is placed on PVC foam and is connected with a 3.5 wt% NaCl solution through a cotton wipe (Fig. 5d). Without the solar intensity input, strong evaporation is extinguished. The water that needs to evaporate is greatly reduced on the top evaporation surface, simultaneously, there is excess water remaining to dissolve water. The accumulated salt crystals start to dissolve and the salt concentration gradient from the upper surface to the lower region of the CI/CS hydrogel evaporator drives the salt down to the underlying bulk water through the water path of interconnected hydrogel networks. The cotton wipe provides a drainage pathway for salt rejecting from the CI/CS hydrogel evaporator to the underlying 3.5 wt% NaCl solution. The dissolving process of the accumulated salt crystals on the top surface was recorded and shown as time-lapse images in Fig. 5e. Around two third of the slat crystals disappear within the first 60 minutes which elucidated the quick salt self-cleaning ability of the CI/CS hydrogel evaporator. All the accumulated salt dissolves in 200 minutes after the solar simulator was off, showing the salt-rejection performance of the CI/CS hydrogel evaporator.

To further exhibit the great salt rejection abilities of the CI/CS hydrogel, 1.5 g NaCl is dispersed on a CI/CS hydrogel with a diameter of 32 mm and a thickness of 7 mm, which is supplied with 3.5 wt% NaCl solution by the cotton wipe underneath, to track the dissolution of salt (Fig. 5f). Time-lapse photographs of the salt-rejection experiment show that the NaCl diffuses completely into the bulk 3.5 wt% NaCl solution within 8 hours with an cotton wipe as a water supply and this validates the salt drainage capability of the CI/CS hydrogel evaporator (Fig. 5g).

The long-term stability and durability of working performance for the evaporator is critical for real-life implementations. As such, the solar desalination experiment with 3.5 wt% NaCl solution is conducted consisting of three 4-hour continuous experiments under one sun irradiation. As shown in Fig. 5h, the evaporation rates stabilize around 4.0 kg m^{-2} h^{-1}, illustrating its long-term working stability. Moreover, the long-term desalination experiment over 8 hours is conducted twice in two consecutive days to test the durability and stability of the CI/CS hydrogel evaporator (Fig. 5i). Each long-term test involves 9 hours which are separated into the first 5.5-hour period and the second 3.5-hour period. For each period, the pre-heating time is required of 0.5 hours, therefore, only the 5-hour and 3-hour stable experimental data are recorded for the first and second period, respectively. After the first 5-hour experiment, the bulk water (3.5 wt% NaCl solution) is replaced to keep the salinity of the water supply constant at 3.5 wt%. This long-time desalination experimental was repeated two times to validate the long-term performance of CI/CS evaporator. A linear mass change of wa-

ter is observed when the CI/CS evaporator is illuminated under one sun for each long-term period, and obviously, the four lines of mass changes almost parallel to each other, which indicates the stability performance of the CI/CS hydrogel evaporator. Additionally, the evaporation rate corresponding to each hour in the long-term test fluctuates between 3.8 kg m^{-2} h^{-1} and 4.1 kg m^{-2} h^{-1}, while also elucidates the long-term durability and stability of the CI/CS evaporator. The evaporator under various solar illumination values is investigated to validate the working performance of CI/CS evaporator under weak or unconcentrated sunlight (Fig. 5j). The evaporation rate of CI/CS hydrogel evaporator under 0.58 suns and 0.8 suns irradiance are 1.9 kg m^{-2} h^{-1} and 2.9 kg m^{-2} h^{-1}, respectively, demonstrating that it is able to work relatively efficiently under weak sunlight. Meanwhile, an evaporation rate of 13.6 kg m^{-2} h^{-1} is demonstrated under 3 suns, extending the scopes of implementations to concentrated solar desalination. Another key point to be concerned is the water quality after desalination. To validate this, seawater collected from Revere Beach, Boston, US is employed to monitor the quality of the water after purification (Fig. 5k). The salinity of water after desalination is dramatically reduced by approximately four orders of magnitude and is two orders of magnitude below the drinking water standards defined by the World Health Organization (1‰) and the US Environmental Protection Agency (0.5‰), respectively. With advantageous features of high evaporation rates in high-salinity water, good salt-dissipation capability, long-time working robustness, and high-quality water yields, the CI/CS hydrogel evaporator display promising indications for scalable applications to seawater desalination.

To validate the out-door working performance of the CI/CS hydrogel-based desalination system under natural sunlight, a controlled experiment for solar desalination test is conducted at the rooftop of Snell Engineering Center at Northeastern University, Boston, MA, USA on July 15, 2021 (Fig. S8 and S9†). The solar desalination system is composed of a sealed condensation chamber and a CI/CS evaporation device with a large area evaporator (9 cm × 9 cm) inside. Details about the setup for the experimental group and control group can be found in the supplementary information. The average ambient temperature and solar intensity are 28.3°C and 744.7 W m^{-2} from 10:30 to 16:00, respectively, during the experimental period. The average freshwater collection rate of the CI/CS evaporation device group is 0.76 kg m^{-2} h^{-1}, while the control group is only 0.10 kg m^{-2} h^{-2}. It is worth noting that the average cost of materials and chemicals for the 3 wt% CI/CS evaporator with thickness of 7 mm is 8.35 USD m^{-2} (Table S4†), which is promising to be applied for high-performance solar desalination systems.

4 Conclusions

In this study, we have demonstrated a full ocean biomass-derived hydrogel photothermal evaporator (CI/CS hydrogel) with interconnected porous channels, achieving a rapid evaporation rate of 4.1 kg m^{-2} h^{-1} under one sun irradiation. The CI/CS-based porous structure is fabricated through the lyophilization of a frozen chitosan and cuttlefish ink hydrogel. The ultra-black cuttlefish ink particles, serving as the photothermal material, ab-

sorb the solar irradiance, and the incident light is also trapped in the porous structure of the chitosan hydrogel. Both of these mechanisms play a key role in achieving the near-unity solar absorptance. The interconnected 3D porous structure allows for rapid water transportation and salt drainage, which are critical for achieving a high evaporation rate and continuous long-term desalination performance. Specifically, the rapid capillary pumping and hydrophilicity from the interconnected channels of the chitosan hydrogel enhance the water diffusion. Additionally, the connection between the microchannels of the chitosan evaporator yields quick replenishment of vaporized brine, which enables the quick and continuous water evaporation and prevents salt accumulation from blocking the water transport. The exceptional heat localization of the CI/CS hydrogel results from its porous structure with low thermal conductivity even in the wet state and the introduction of both the cotton wipe as the water path and PVC foam as a thermal barrier to restrict the heat diffusion from the hydrogel to the bulk water beneath. A rapid evaporation rate of 13.6 kg m^{-2} h^{-1} is attained under 3 suns irradiation, exhibiting its potential for working under concentrated sunlight without salt accumulations. The salinity of the evaporated water is lower than the freshwater standard of both WHO and EPA, which supports its application as a widespread system to enhance the availability of fresh water. Taking advantage of the abundant and sustainable raw materials chitosan and cuttlefish ink while yielding a high evaporation rate, this CI/CS hydrogel evaporator displays great promise for eco-friendly and scalable clean water production from various water sources, such as seawater, sewage, and high-salinity brines.

Author contributions

X.L., Y.T., and Y.Z. conceived the initial concept. X.L., F.C., and Y.W. performed desalination experiments in lab. A.C., S.C., Y.W., and J.D. conducted characterization experiments and analyzed the corresponding data. All authors discussed the results and commented on the manuscript. Y.Z. supervised this project.

Conflicts of interest

There are no conflicts to declare.

Acknowledgements

Notes and references

1 M. M. Mekonnen and A. Y. Hoekstra, *Science advances,* 2016, **2**, e1500323.

2 S. Wang, Y. Fan, F. Wang, Y. Su, X. Zhou, Z. Zhu, H. Sun, W. Liang and A. Li, *Desalination*, 2021, **505**, 114982.

3 Z. Li, X. Ma, D. Chen, X. Wan, X. Wang, Z. Fang and X. Peng, *Advanced Science*, 2021, 2004552.

4 K. Liu, W. Zhang, H. Cheng, L. Luo, B. Wang, Z. Mao, X. Sui and X. Feng, *ACS Applied Materials & Interfaces*, 2021.

5 J. Li, X. Wang, Z. Lin, N. Xu, X. Li, J. Liang, W. Zhao, R. Lin, B. Zhu, G. Liu *et al.*, *Joule*, 2020, **4**, 928–937.

6 N. Xu, J. Li, Y. Wang, C. Fang, X. Li, Y. Wang, L. Zhou, B. Zhu, Z. Wu, S. Zhu *et al.*, *Science advances*, 2019, **5**, eaaw7013.

7 C. Zhang, Y. Shi, L. Shi, H. Li, R. Li, S. Hong, S. Zhuo, T. Zhang and P. Wang, *Nature Communications*, 2021, **12**, 1–10.

8 Y. Xia, Y. Kang, Z. Wang, S. Yuan, Y. Li, L. Gao, H. Wang and X. Zhang, *Journal of Materials Chemistry A*, 2021, **9**, 6612–6633.

9 L. Zhou, Y. Tan, J. Wang, W. Xu, Y. Yuan, W. Cai, S. Zhu and J. Zhu, *Nature Photonics*, 2016, **10**, 393–398.

10 X. Zhang, X. Wang, W. D. Wu, X. D. Chen and Z. Wu, *Journal of Materials Chemistry A*, 2019, **7**, 6963–6971.

11 F. Wang, D. Wei, Y. Li, T. Chen, P. Mu, H. Sun, Z. Zhu, W. Liang and A. Li, *Journal of Materials Chemistry A*, 2019, **7**, 18311–18317.

12 C. Tu, W. Cai, X. Chen, X. Ouyang, H. Zhang and Z. Zhang, *Small*, 2019, **15**, 1902070.

13 F. Meng, B. Ju, S. Zhang and B. Tang, *Journal of Materials Chemistry A*, 2021.

14 X. Zhou, Y. Guo, F. Zhao and G. Yu, *Accounts of chemical research*, 2019, **52**, 3244–3253.

15 W. Xu, Y. Xing, J. Liu, H. Wu, Y. Cui, D. Li, D. Guo, C. Li, A. Liu and H. Bai, *ACS nano*, 2019, **13**, 7930–7938.

16 Y. Wang, L. Zhang and P. Wang, *ACS Sustainable Chemistry & Engineering*, 2016, **4**, 1223–1230.

17 C. Li, D. Jiang, B. Huo, M. Ding, C. Huang, D. Jia, H. Li, C.-Y. Liu and J. Liu, *Nano Energy*, 2019, **60**, 841–849.

18 P. Sun, W. Zhang, I. Zada, Y. Zhang, J. Gu, Q. Liu, H. Su, D. Pantelic, B. Jelenkovic and D. Zhang, *ACS applied materials & interfaces*, 2019, **12**, 2171–2179.

19 L. Yang, G. Chen, N. Zhang, Y. Xu and X. Xu, *ACS Sustainable Chemistry & Engineering*, 2019, **7**, 19311–19320.

20 J. Li, X. Zhou, P. Mu, F. Wang, H. Sun, Z. Zhu, J. Zhang, W. Li and A. Li, *ACS applied materials & interfaces*, 2019, **12**, 798–806.

21 Q. Fang, T. Li, Z. Chen, H. Lin, P. Wang and F. Liu, *ACS applied materials & interfaces*, 2019, **11**, 10672–10679.

22 S. Cao, P. Rathi, X. Wu, D. Ghim, Y.-S. Jun and S. Singamaneni, *Advanced Materials*, 2020, 2000922.

23 S. He, C. Chen, Y. Kuang, R. Mi, Y. Liu, Y. Pei, W. Kong, W. Gan, H. Xie, E. Hitz *et al.*, *Energy & Environmental Science*, 2019, **12**, 1558–1567.

24 Y. Kuang, C. Chen, S. He, E. M. Hitz, Y. Wang, W. Gan, R. Mi and L. Hu, *Advanced materials*, 2019, **31**, 1900498.

25 M. M. Ghafurian, H. Niazmand, E. Ebrahimnia-Bajestan and R. A. Taylor, *Renewable Energy*, 2020, **146**, 2308–2315.

26 P. He, L. Hao, N. Liu, H. Bai, R. Niu and J. Gong, *Chemical Engineering Journal*, 2021, **423**, 130268.

27 M. Zhu, A. Xia, Q. Feng, X. Wu, C. Zhang, D. Wu and H. Zhu, *Energy Technology*, 2020, **8**, 1901215.

28 N. Xu, X. Hu, W. Xu, X. Li, L. Zhou, S. Zhu and J. Zhu, *Advanced Materials*, 2017, **29**, 1606762.

29 D. P. Storer, J. L. Phelps, X. Wu, G. Owens, N. I. Khan and H. Xu, *ACS applied materials & interfaces*, 2020, **12**, 15279–15287.

30 P. M. Pakdel and S. J. Peighambardoust, *Carbohydrate polymers*, 2018, **201**, 264–279.

31 M. C. Pellá, M. K. Lima-Tenório, E. T. Tenório-Neto, M. R. Guilherme, E. C. Muniz and A. F. Rubira, *Carbohydrate Polymers*, 2018, **196**, 233–245.

32 Y. Zhang, B. Dong, A. Chen, X. Liu, L. Shi and J. Zi, *Advanced Materials*, 2015, **27**, 4719–4724.

33 Y. Zhang and M. Zhang, *Journal of Biomedical Materials Research: An Official Journal of The Society for Biomaterials, The Japanese Society for Biomaterials, and The Australian Society for Biomaterials and the Korean Society for Biomaterials*, 2002, **62**, 378–386.

34 M. R. Kumar, R. Muzzarelli, C. Muzzarelli, H. Sashiwa and A. Domb, *Chemical reviews*, 2004, **104**, 6017–6084.

35 R. Muzzarelli and C. Muzzarelli, *Polysaccharides I*, 2005, 151–209.

36 M. Dash, F. Chiellini, R. M. Ottenbrite and E. Chiellini, *Progress in polymer science*, 2011, **36**, 981–1014.

37 S. Ahmed and S. Ikram, *Chitosan: derivatives, composites and applications*, John Wiley & Sons, 2017.

38 J. Mendelsohn, P. M. Howley, M. A. Israel, J. W. Gray and C. B. Thompson, *The Molecular Basis of Cancer E-Book*, Elsevier Health Sciences, 2014.

39 C. Lustriane, F. M. Dwivany, V. Suendo and M. Reza, *Journal of Plant Biotechnology*, 2018, **45**, 36–44.

40 J. Schmaler-Ripcke, V. Sugareva, P. Gebhardt, R. Winkler, O. Kniemeyer, T. Heinekamp and A. A. Brakhage, *Applied and environmental microbiology*, 2009, **75**, 493–503.

41 X. Li, J. Li, J. Lu, N. Xu, C. Chen, X. Min, B. Zhu, H. Li, L. Zhou, S. Zhu *et al.*, *Joule*, 2018, **2**, 1331–1338.

42 B. Ratajska-Gadomska and W. Gadomski, *The Journal of chemical physics*, 2004, **121**, 12583–12588.

43 F. Zhao, X. Zhou, Y. Shi, X. Qian, M. Alexander, X. Zhao, S. Mendez, R. Yang, L. Qu and G. Yu, *Nature nanotechnology*, 2018, **13**, 489–495.

44 Y. Gu, X. Mu, P. Wang, X. Wang, J. Liu, J. Shi, A. Wei, Y. Tian, G. Zhu, H. Xu *et al.*, *Nano Energy*, 2020, **74**, 104857.

45 Y. Gu, X. Mu, P. Wang, X. Wang, Y. Tian, A. Wei, J. Zhang, Y. Chen, Z. Sun, J. Zhou *et al.*, *Global Challenges*, 2021, **5**, 2000063.

46 X. Hu, W. Xu, L. Zhou, Y. Tan, Y. Wang, S. Zhu and J. Zhu, *Advanced materials*, 2017, **29**, 1604031.

47 Y. Xu, X. Xiao, X. Fan, Y. Yang, C. Song, Y. Fan and Y. Liu, *Journal of Materials Chemistry A*, 2020, **8**, 24108–24116.

48 F. Yu, Z. Guo, Y. Xu, Z. Chen, M. S. Irshad, J. Qian, T. Mei and X. Wang, *ACS Applied Materials & Interfaces*, 2020.

49 L. Yang, N. Li, C. Guo, J. He, S. Wang, L. Qiao, F. Li, L. Yu, M. Wang and X. Xu, *Chemical Engineering Journal*, 2020, 128051.

50 C. Liu, K. Hong, X. Sun, A. Natan, P. Luan, Y. Yang and H. Zhu, *Journal of Materials Chemistry A*, 2020, **8**, 12323–12333.

51 M. S. Irshad, X. Wang, M. S. Abbasi, N. Arshad, Z. Chen, Z. Guo, L. Yu, J. Qian, J. You and T. Mei, *ACS Sustainable Chemistry & Engineering*, 2021.

52 A. M. Saleque, S. Ma, S. Ahmed, M. I. Hossain, W. Qarony and Y. H. Tsang, *Advanced Sustainable Systems*, 2021, 2000291.

53 L. Song, X.-F. Zhang, Z. Wang, T. Zheng and J. Yao, *Desalination*, 2021, **507**, 115024.